$(Ba_{0.85}Ca_{0.15})(Ti_{0.9}Zr_{0.1})O_3$ thin films prepared by PLD: Relaxor properties and complex microstructure

André Piorra, Viktor Hrkac, Niklas Wolff (iD), Christiane Zamponi, Viola Duppel, Joke Hadermann, Lorenz Kienle, and Eckhard Quandt

View Online   **Export Citation**   **CrossMark**

ARTICLES YOU MAY BE INTERESTED IN

Mapping the structural transitions controlled by the trilinear coupling in $Ca_{3-x}Sr_xTi_2O_7$
Journal of Applied Physics **125**, 244102 (2019); https://doi.org/10.1063/1.5089723

$BaTiO_3$-based piezoelectrics: Fundamentals, current status, and perspectives
Applied Physics Reviews **4**, 041305 (2017); https://doi.org/10.1063/1.4990046

Structural phase diagram and magnetic properties of Sc-substituted rare earth ferrites $R_{1-x}Sc_xFeO_3$ (R = Lu, Yb, Er, and Ho)
Journal of Applied Physics **125**, 244101 (2019); https://doi.org/10.1063/1.5098488

$(Ba_{0.85}Ca_{0.15})(Ti_{0.9}Zr_{0.1})O_3$ thin films prepared by PLD: Relaxor properties and complex microstructure

André Piorra,[1] Viktor Hrkac,[2] Niklas Wolff,[2] [ID] Christiane Zamponi,[1] Viola Duppel,[3] Joke Hadermann,[4] Lorenz Kienle,[2] and Eckhard Quandt[1,a)]

AFFILIATIONS

[1]Inorganic Functional Materials, Faculty of Engineering, Kiel University, 24143 Kiel, Germany
[2]Synthesis and Real Structure, Faculty of Engineering, Kiel University, 24143 Kiel, Germany
[3]Max Planck Institute for Solid State Research, 70569 Stuttgart, Germany
[4]EMAT, Department of Physics, University of Antwerp, 2020 Antwerpen, Belgium

[a)]Electronic mail: eq@tf.uni-kiel.de

ABSTRACT

Ferroelectric lead-free thin films of the composition $(Ba_{0.85}Ca_{0.15})(Ti_{0.9}Zr_{0.1})O_3$ (BCZT) were deposited by pulsed laser deposition on $Pt/TiO_2/SiO_2/Si$ substrates using a ceramic BCZT target prepared by a conventional solid state reaction. The target material itself shows a piezoelectric coefficient of $d_{33} = 640$ pm/V. The (111) textured thin films possess a thickness of up to $1.1\,\mu m$ and exhibit a clamped piezoelectric response $d_{33,f}$ of up to 190 pm/V, a dielectric coefficient of $\varepsilon_r = 2000$ at room temperature, and a pronounced relaxor behavior. As indicated by transmission electron microscopy, the thin films are composed of longitudinal micrometersized columns with $\sim$100 nm lateral dimension that are separated at twin- and antiphase boundaries. The superposition phenomena according to this columnar growth were simulated based on suitable supercells. The major structural component is described as a tetragonal distorted variant of the perovskite parent type; however, frequently coherently intergrown nanodomains were observed indicating a much more complex structure that is characterized by a 7-layer modulation along the growth direction of the films.

INTRODUCTION

Ferroelectric thin films with high piezoelectric coefficients are attractive for many sensor and actuator applications.[1–3] Despite the toxicity of lead containing compounds, most of these applications are based on the excellent piezoelectric properties of lead zirconate titanate (PZT) and its compounds.[4] Legal restrictions to replace lead by nontoxic materials have led to significant achievements in the preparation of high performance lead-free ferroelectric and especially piezoelectric materials in recent years.[5–7] Despite the great variety of promising lead-free materials, thin films made of lead-free ferroelectric materials still show a comparable lower piezoelectric response. Effective piezoelectric coefficients in the range of around $d_{33,f} = 60$ pm/V were found for films of tantalum substituted $K_{0.5}Na_{0.5}NbO_3$ or $Bi_{3.15}Dy_{0.85}Ti_3O_{12}$ being thus around two times lower than for state of the art thin

films of PZT.[8–10] A more promising candidate was recently identified to be the compound $(Ba_{0.85}Ca_{0.15})(Ti_{0.9}Zr_{0.1})O_3$ (BCZT). The piezoelectric coefficient of $d_{33} = 620$ pC/N for BCZT bulk ceramics was reported to be close to the one of PZT.[11] However, the piezoelectric constant d_{33} of bulk ceramics is significantly higher than the effective $d_{33,f}$ of thin films due to the clamping of the film by the substrate.[12] The effective piezoelectric constant $d_{33,f}$ of a clamped thin film on a substrate can be estimated based on the following formula:[13]

$$d_{33,f} = d_{33} - \frac{2\,S_{13}^E}{S_{11}^E + S_{12}^E} \cdot d_{31}, \tag{1}$$

with d_{31} and d_{33} the piezoelectric coefficients and S_{ij}^E of the bulk material.

TABLE I. Piezoelectric and elastic constants for BCZT[11,15] and PZT.[16]

	d_{31}/pC/N	d_{33}/pC/N	d_{33}/pm/V	S_{11}^E/10^{-12} Pa^{-1}	S_{12}^E/10^{-12} Pa^{-1}	S_{13}^E/10^{-12} Pa^{-1}
BCZT	−231	546	1140	15.5	−5.5	−7.4
PZT	−93.5	223	900	13.8	−4.01	−5.8

Following Eq. (1) and using the materials constants of BCZT given in Table I, one can assume an effective piezoelectric constant $d_{33,f} = 203$ pm/V for thin films. This would be a considerably higher piezoelectric constant compared to the expected value for PZT ($d_{33,f} = 168$ pm/V).[14] Calculations based on the piezoelectric coefficient of the converse effect and under the assumption that the d_{31} scales with the same ratio provide a theoretical coefficient of $d_{33,f} = 427$ pm/V and demonstrate the enormous potential of BCZT films.

Published experimental values of the piezoelectric coefficient for films of BCZT are indeed promising.

Thin films prepared by a chemical solution deposition process show piezoelectric coefficients of $d_{33,f} = 1.1$ pm/V,[17] a $d_{33,f} = 104$ pm/V,[18] or a $d_{33,f} = 141$ pm/V.[19] Reported values for films prepared by other deposition methods, like magnetron sputtering ($d_{33,f} = 94$ pm/V[20]) and pulsed laser deposition ($d_{33,f} = 80$ pm/V[21]), show similar piezoelectric response.

Ferroelectric BCZT bulk ceramics exhibit a sharp transition from the ferroelectric tetragonal phase to the paraelectric cubic phase with a Curie temperature, $T_C = 93\,°C$.[11] However, several reports on thin films of BCZT give the presumption of a relaxor behavior.[22,23] In general, the substitution of Ti ions by Zr ions is seen as a key factor for a transition from a ferroelectric phase transition to a relaxor state.[24,25] The main characteristic of a relaxor is the pronounced diffuse change in permittivity ε at temperatures near transition,[26,27] whereby the maximum of the dielectric constant ε_M at T_m shows a dependence of frequency f according to the Vogel-Fulcher relationship following the equation:[28]

$$f = f_0 \cdot \exp\left(\frac{-E_A}{k_B(T_m - T_f)}\right), \qquad (2)$$

where E_A is the activation energy, k_B is the Boltzmann constant, T_f is the Vogel-Fulcher temperature, and f_0 an attempt frequency.

Similar to ferroelectrics, relaxor materials show a paraelectric phase at high temperatures. Ferroelectrics transform at the Curie temperature T_C into the paraelectric phase near the maximum of the dielectric constant ε_M associated with a structural change. A relaxor material possesses a polarization unequal to zero above ε_M until the Burns temperature T_B is reached, where the polarization becomes zero and the material will be in a paraelectric state without a change in the crystal structure.[29] Between ε_M and T_B, the dielectric constant ε follows a modified Curie-Weiss law in dependence of the temperature proposed by Uchino et al.,[30]

$$\frac{1}{\varepsilon} - \frac{1}{\varepsilon_M} = \frac{(T - T_M)^\gamma}{C'}, \qquad (3)$$

with γ and C' being constants. The parameter γ describes the diffuse character of the transition and ranges between 1 and 2; for

$\gamma = 1$, a normal ferroelectric material is observed, and for $\gamma = 2$, a complete diffuse transition is seen.[31,32]

Closely related to the appearance of relaxor behavior is the existence of polar nanoregions (polar nanodomains). By cooling, they transform from the nonpolar paraelectric phase at the Burns temperature, T_B, to nanometer scale polar regions with randomly oriented dipole moments. The relaxor exists in the ergodic state, where external forces (electrical fields or mechanical stress) could transform it reversely into a ferroelectric state. With decreasing temperature, the mobility of the polar nanodomains decreases. At the temperature T_f, the nanodomains are frozen in and the relaxor is transformed into a nonergodic state. In this state, the relaxor can irreversibly be transformed into a ferroelectric state by applying sufficiently strong external fields.[25,29]

Despite first studies on the nanostructure of bulk samples from BCZT,[33] a lack of in-depth analyses of BCZT thin film samples must be stated. In this work, we discuss the di- and piezoelectric properties of BCZT thin films, which are associated with the characteristics of a relaxor. Nanostructural features have been investigated by methods of transmission electron microscopy (TEM) and evaluated using computational approaches.

EXPERIMENTAL

Thin film fabrication

A ceramic target of BCZT was prepared by a conventional solid state reaction starting from pure powders followed by sintering to solid targets (size: 20 mm in diameter). More details of the preparation of the target material can be found in Ref. 21. A pulsed laser deposition workstation manufactured by Surface System & Technology GmbH & Co. KG was used to prepare the BCZT thin films utilizing a KrF laser with a wavelength of 248 nm and energy of 350 mW. The platinized silicon substrates were prepared by sputtering (von Ardenne CS730S sputtering system) a 150 nm thick platinum film on thermally oxidized silicon wafers [Si (100)] with a power of 20 W without additional heating. A 10 nm thick sputter deposited titanium film was used as diffusion barrier. Deposition of ~900 nm thick BCZT thin films was carried out at a laser frequency of 10 Hz and an oxygen partial pressure of 0.14 mbar on 10 mm by 10 mm pieces of platinized silicon at a deposition temperature of 800 °C. The target to substrate distance was set to 50 mm and 40 mm. Subsequently, the films were cooled down to room temperature at an oxygen partial pressure of 3 mbar. The deposition rate was determined to be 0.12 nm/pulse.

Thin film characterization

The microstructures of the thin films were characterized by X-ray diffraction (XRD) (Seifert XRD 3003 PTS). The structuring

of Au electrodes for measuring the piezo- and ferroelectric properties was done via sputtering and photolithographic etching followed by a lift-off process. Thin films and bulk ceramics were characterized with a double beam laser interferometer (DBLI) (aixDBLI, Aixacct).

TEM investigations

The structural analysis on samples deposited at a substrate to a target distance of 50 mm was carried out using three different TEMs: (1) a FEI Tecnai F30 G^2 STwin operated at 300 kV [field emission gun (FEG), spherical aberration coefficient C$_S$ = 1.2 mm] and (2) a Philips CM 30 ST microscope (LaB$_6$ cathode, 300 kV, C$_S$ = 1.15 mm) were used for electron diffraction analysis, (3) a FEI Titan 80–300 "cubed" microscope equipped with a Super-X EDX detector and operated at 200 kV was used for high resolution scanning transmission electron microscopy (HRSTEM) images and STEM-EDX elemental maps. A thin lamella of BCZT was prepared by focused ion beam (FIB) milling using a lift-out method with an FEI Helios Nanolab system. Selected area electron diffraction (SAED) patterns were obtained using a radial aperture, which limited the diffraction to an area of 250 nm (Tecnai F30) and 100 nm (Philips) in diameter. All high resolution (HR)TEM micrographs and ED pattern were evaluated with the program Digital Micrograph 3.6.1 (Gatan, Inc.) (DM). Simulations of SAED patterns were calculated using the JEMS program package.[34] For contrast enhancement of HRTEM micrographs, the HRTEM filter plug-in for DM was applied.[35] Due to the small variations in the lattice parameters of BCZT for the possible phases[9,36] and to simplify the discussion of crystallographic orientations, cubic metrics (labeled by "C") will be used for the notation of the presented miller indices. An exception is the symmetry discussion for the convergent beam electron diffraction (CBED) studies.

RESULTS AND DISCUSSION
Morphology and real structure of major component

Experimentally obtained XRD patterns (see Fig. 1) exhibit a strong (111)$_c$ texture of BCZT films (FWHM of 1.3°) on a preferably (111) oriented Pt seed layer (FWHM of 1.4°). Only marginal intensity is observed for other planes as (100)$_c$ and (110)$_c$. This result proves the absence of secondary crystalline phases; however,

the precise determination of metrics and symmetry is not feasible by XRD. The highly oriented growth represents a clear improvement compared to the previous work.[21] The strongly textured (111)$_c$ growth on (111) oriented Pt films on silicon is well known for BaTiO$_3$ (BTO) films prepared by pulsed laser deposition due to the small lattice mismatch of Pt and BTO.[37]

Dielectric and piezoelectric properties

The (111) orientation of the BTO films is favorable for a maximum piezoelectric coefficient as shown by calculations from Davis et al.[38] and Ouyang et al.[39] These calculations where confirmed by Li et al. via investigations on Ba$_{0.98}$Ca$_{0.02}$Ti$_{0.96}$Sn$_{0.04}$O$_3$ thin films with different preferred orientations. For (111) and (100) oriented films, the authors found a piezoelectric coefficient of $d_{33,f} = 78$ pm/V and $d_{33,f} = 36$ pm/V,[40] respectively. As BCZT is based on BTO it is thus assumed that the (111) orientation is also the most favorable orientation in BCZT.

The dielectric and piezoelectric properties of the BCZT film are depicted in Fig. 2. A narrow ferroelectric hysteresis is observed [Fig. 2(a)] with low coercive fields and only a small coercivity in the C(apacitance)-V(oltage) curves. Additionally, a maximum dielectric permittivity of $\varepsilon = 2000$ at 5 kHz and room temperature was measured being within the broad range of reference values reaching from $\varepsilon = 259$[18] to $\varepsilon = 2913$[17] reported for BCZT thin films [Fig. 2(b)]. The dielectric measurements demonstrate a shift of the field characteristics, which was already noted in previous studies[21] as imprint. A preference of one polarization state over the other leading to a shift of the ferroelectric hysteresis on the voltage axes.[41,42] Oxygen loss gradients inside the film arising during preparation or mechanical stress inside the film could be responsible for this imprint behavior.[43–45] Besides this, extrinsic effects due to different electrode materials, on bottom, we use Platinum, on top, Chromium and Gold could also lead to this behavior due to the different work functions.[46,47]

Furthermore, the BCZT films exhibit a giant piezoelectric response with respect to other lead-free ferroelectric thin films,[21] possessing a maximum effective piezoelectric constant of more than $d_{33,f} = 190$ pm/V [Fig. 2(c)], exceeding the PZT value, but showing a discontinuous variation across the entire film. Areas with an effective piezoelectric constant of $d_{33,f} = 190$ pm/V and
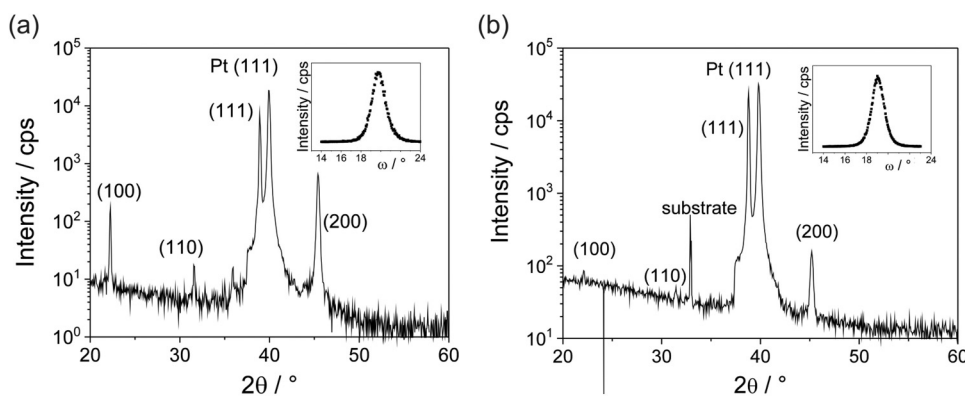

FIG. 1. XRD scans of BCZT thin films deposited at a substrate to target distance of (a) 50 mm and (b) 40 mm. The full width-at-half maxima of the (111) intensities are 1.55° and 1.3° and show the strong texture of the films, respectively.
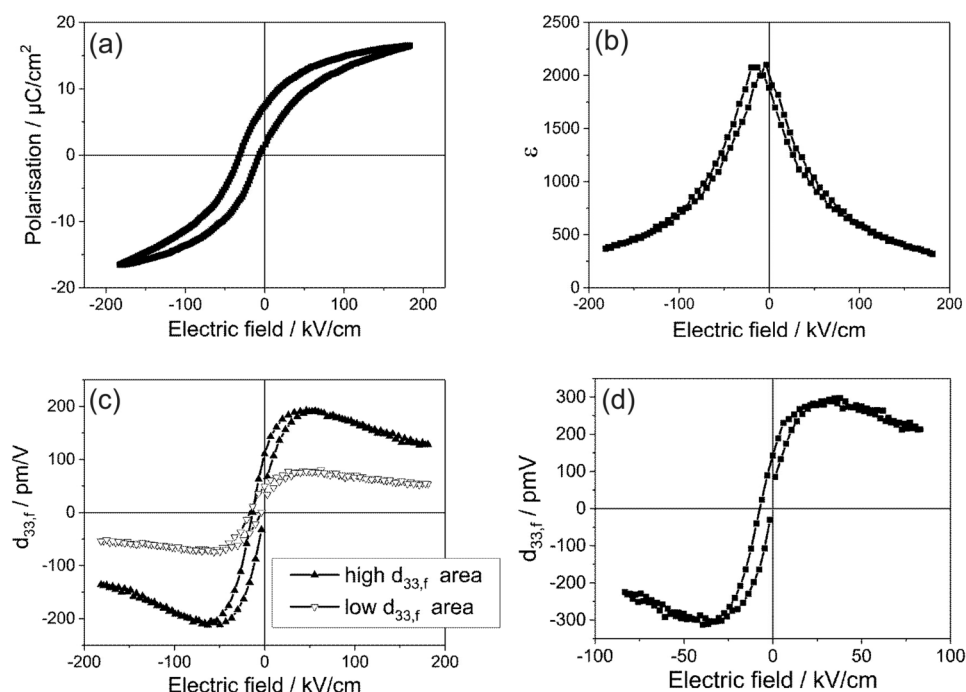
FIG. 2. Di- and piezoelectric properties of BCZT thin films. (a) Ferroelectric hysteresis, (b) dielectric permittivity vs voltage, (c) piezoelectric coefficient $d_{33,f}$ vs voltage of different positions on the sample at 50 mm substrate to target distance and (d) piezoelectric coefficient $d_{33,f}$ vs voltage for 40 mm substrate to target distance.

with $d_{33,f} = 80$ pm/V in maximum were detected; please note that the $d_{33,f}$ values within a given area are constantly high or low. Interestingly, by decreasing the substrate to target distance from 50 mm to 40 mm, the maximum effective piezoelectric coefficient could be increased up to $d_{33,f} = 300$ pm/V in maximum [Fig. 2(d)], marking one of the highest values reported for lead-free piezoelectric films. However, the origin of the discontinuous variation and higher piezoelectric coefficient is highly speculative up to date and is a topic for future research. Multiple factors which were reported to influence the piezoelectric coefficients concern the quality of the microstructure, e.g., crystal orientation,[18] crystal structure and chemical composition around the morphotropic phase boundary,[11,48,49] the grain size,[50] interfacial strain and dislocation density,[51] film thickness,[52] as well as speculations about the density of polar nanodomains responsible for the relaxor effect seems reasonable.[53]

BCZT ceramics introduced as the ferroelectric material show a sharp transition from the ferroelectric tetragonal phase to the paraelectric cubic phase.[11] The temperature dependence of the dielectric permittivity within a frequency range from kilohertz to megahertz is investigated for the BCZT films with a substrate target distance of 50 mm, [cf. Fig. 3(a)]. The recorded curves are characterized by a broad peak and thus do not express a clear defined maximum. From these data, the characteristic transition is, therefore, hard to identify, which is contrary to the distinct phase transition of the bulk ceramic. Indeed, own investigations on BCZT bulk ceramics show clear ferroelectric characteristics as depicted in Fig. S2 of the supplementary material.

Furthermore, BCZT films show a temperature shift of the maximum value for the dielectric constant ε_M when applying different frequencies during the respective measurements [cf. Fig. 3(a)].

For the performed experiments, the peak temperature values T_M corresponding to $\varepsilon_M(f)$ are in the range from 326 K (53 °C) to 334 K 61 °C. Such findings serve as an indication for a relaxor behavior. Additional validation for this hypothesis is deducible from the deviation of the linear Curie-Weiss law near and above ε_M at 10 kHz as presented in Fig. 3(b). Starting from 360 K (87 °C), a linear behavior according to the Curie-Weiss law is visible. The diffuse region below the paraelectric part and above ε_M can be described by using the modified Curie-Weiss law [Eq. (3)]. Replotting the same data within modified axes {y = $\ln\left(\frac{1}{\varepsilon} - \frac{1}{\varepsilon_M}\right)$ and x = $\ln(T - T_M)$ [Fig. 3(c)]}, the degree of diffuseness γ is determined to be $\gamma = 2$, confirming an ideal relaxor behavior.[30] Following the phenomenology of a relaxor material, the temperature of 360 K sets the Burns temperature T_B, i.e., the transition from the high temperature paraelectric phase to the state of an ergodic relaxor. A particularity at T_B is the appearance of mobile polar nanodomains and the decrease of this mobility during a cooling process. At a certain temperature, the nanodomains are frozen. According to the Vogel-Fulcher-law, this freezing temperature can be calculated by fitting the temperature dependent maxima of the dielectric permittivity in dependence of the frequency.[25,29] Additionally, the implementation of the Vogel-Fulcher law is a criterion for the complete crossover from a ferroelectric to a relaxor state.[25] Figure 3(d) shows $\ln f$ as a function of T_M and the fitted values using the Vogel-Fulcher relationship [Eq. (2)]. A Vogel-Fulcher temperature as expression for the freezing of polar nanodomains was identified at $T_{V-F} = 303$ K.

Similar relaxor behavior of BCZT thin films was observed in other studies. For instance, Bhardwaj *et al.* reported about the relaxor behavior of BCZT films prepared by pulsed laser deposition. A diffuseness parameter of $\gamma = 1.88$ and a dependence of the maximum
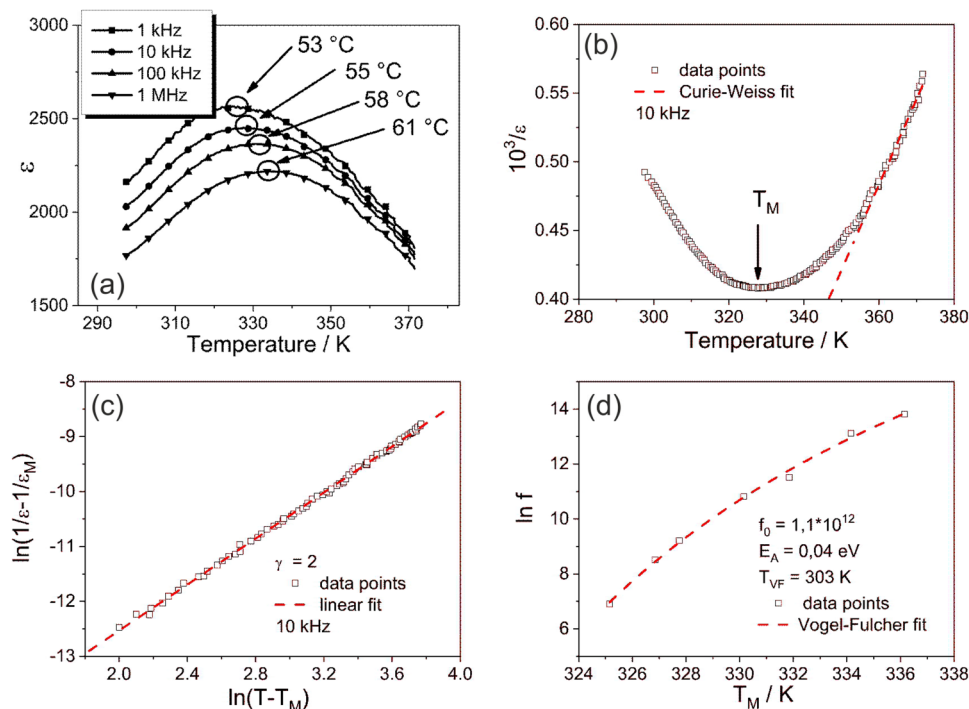
FIG. 3. Relaxor properties of BCZT thin films. (a) Temperature dependence of dielectric constant at different frequencies, (b) reciprocal dielectric constant as function of the temperature at 10 kHz, fits shows the range of validity of the Curie-Weiss law, (c) modified Curie-Weiss law fit of values, and (d) fit of measured values according to Vogel-Fulcher relation shift.

of the dielectric constant ε_M according to the Vogel-Fulcher law was found, and a Vogel-Fulcher temperature of $T_{V-F} = 329.7\,\text{K}$ was determined.[22] For sol-gel prepared thin films with the discussed composition of BCZT, Lin *et al.* found a matching of the Vogel-Fulcher relationship with a Vogel-Fulcher temperature of $T_{V-F} = 315\,\text{K}$ and a diffuseness parameter of $\gamma = 1.98$.[23]

In these cases, the origin of the relaxor behavior was explained by the simultaneous substitution of Ca^{2+} on Ba^{2+} sites and Zr^{4+} on Ti^{4+} sites of the $BaTiO_3$ host lattice.[22,23]

However, the simultaneous substitution is only one possible option of the four. The second and third options are the homovalent substitution of Zr^{4+} ions on Ti^{4+} sites or either Ca^{2+} ions on Ba^{2+} sites. The fourth option describes the heterovalent substitution of Ca^{2+} ions on Ti^{4+} sites. Each option leads to structural and charge inhomogeneities. These structural and charge inhomogeneities cause the appearance of polar nanodomains and are closely related to a relaxor behavior.

In classical relaxor materials such as PMN these inhomogeneities result from the coexistence of the two B-site ions Mg^{2+} and Nb^{5+}. These heterovalent cations are inhomogeneously distributed and form chemically ordered regions which are surrounded by disordered regions and act as sources for random electric fields.[25] These fields are proposed to be the origin of a relaxor behavior.[54]

The origin of random fields and by that the explanation of a ferroelectric-relaxor crossover in homovalent substituted compositions like in $BaTi_{1-x}Zr_xO_3$ differs from the heterovalent case due to the absence of any charge disorder. The ferroelectric polarization in pure BTO results mainly from the off-centre shifts of the Ti^{4+} ions.[25] That is, Zr^{4+} ions on Ti^{4+} sites cannot go off-centre due to their larger radius, thus breaking of the cooperative displacement of the Ti-O-Ti-O chains.[40] Such a broken-bond-type state changes in the course of a higher degree of substitution into a predominately random-field-type disorder.[25] This disorder is due to the distortion around Zr^{4+} ions and interrelated redistributions of charges and local formation of charged centres.

The substitution of Zr^{4+} on Ti^{4+} positions of BTO leads indeed to a complete crossover from a ferroelectric to a relaxor state, as reported for bulk ceramics[24,29] and thin films.[55] However, the critical concentration of Zr for a ferroelectric-relaxor crossover in $BaTi_{1-x}Zr_xO_3$ substituted ceramics is found to be $x = 30$ at. %.[25] Dixit *et al.* investigated thin films of $BaTi_{1-x}Zr_xO_3$ in the range $0.3 \leq x \leq 0.7$ and found a maximum of the diffusivity for the composition $BaZr_{0.40}Ti_{0.60}O_3$ with $\gamma = 1.8$ at the fulfilment of the Vogel-Fulcher law simultaneously.[31]

The above discussed BCZT composition contains 10 at. % of Zr. Thus, the role of substituent Ca^{2+} attaches high importance. A homovalent substitution of Ca^{2+} ions on B-sites could also generate random electric fields. Ca^{2+} ions are smaller than Ba^{2+} ions and are able to occupy off-centre positions on the A-site. Additionally, Ca^{2+} ions can substitute B-site positions.[56] Victor *et al.* found that films of $Ba_{1-x}Ca_xTiO_3$ which were prepared by pulsed laser deposition on platinized silicon substrates exhibit a relaxorlike behavior with increasing Ca^{2+} ion content.[57] For a concentration $x = 12$ at. % of Ca^{2+}, a behavior according to the Vogel-Fulcher law was obtained, and the parameter γ was determined to be $\gamma = 1.78$. The effect was explained by the substitution of Ca^{2+} ions on Ti^{4+} sites. The substitution of Ca^{2+} on Ti^{4+}-sites was demonstrated by Park *et al.* and Krishna *et al.*[58,59] A substitution can occur for compositions with a

molar ratio (Ba + Ca) / Ti = 1 and not only for compositions with a molar ratio (Ba + Ca)/Ti > 1 with an excess of Ca.[59] A solubility limit of 3 mol. % was found at a temperature 1450 °C for the BTO ceramic.[60] Due to the substitution of Ca^{2+} on Ti^{4+} sites, a neighboring O^{2-} ion forms a vacancy to balance the charge misfit and Ca^{2+}-V_O dipoles result.[56]

A homovalent substitution leads to weaker random fields than a heterovalent substitution.[54] Due to the relatively low substituent content of the investigated BCZT films in comparison to pure Zr substituted BTO based relaxor materials, one can argue that the substitution of Ca^{2+} ions on Ti^{4+} sites, which has the character of a heterovalent substitution, leads to the observed pronounced relaxor behavior. Additionally, first-principle calculations on homovalent substituted compositions of $BaTi_{0.74}Zr_{0.26}O_3$ by Laulhé et al. have shown that the displacement of Ti^{4+} ions is not only restricted to the $\langle 111 \rangle$ directions but also does appear for the $\langle 100 \rangle$ and $\langle 110 \rangle$ directions. The authors argued that these findings are also applicable for other BTO based homovalent substituted

relaxors.[61] The higher degree of polarization directions links not only the formation of polar nanodomains[61] but could also give an explanation for the excellent piezoelectric properties of the investigated BCZT films.

TEM investigations

Thin films of BCZT were studied in the following. The morphology [Fig. 4(a)] is characterized by columnar BCZT grains (~150 nm in lateral dimension) which are extended perpendicularly to the substrate-BCZT interface with a more or less pronounced wedge shape of these columns. A preferred growing direction of the columns was observed along the $[111]_c$ direction using electron diffraction and Fourier transformations of HRTEM micrographs, confirming the XRD results. Applying CBED, a more reliable identification of the slight deviations from the cubic symmetry of the structure is possible by carefully analyzing the intensity of the diffraction disks, which revealed symmetry with the two
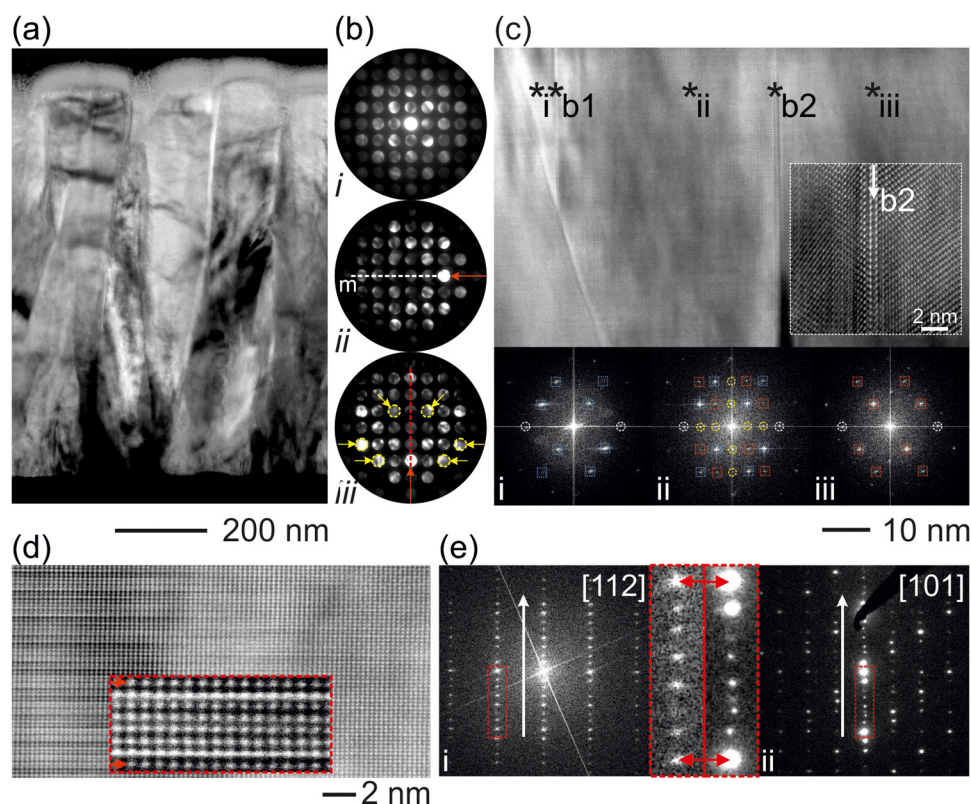

FIG. 4. Structural observations of the BCZT layer. (a) TEM bright field image of a cross-sectional view of BCZT. (b) Representative CBED symmetry study of a single grain: CBED pattern along the $[100]_C$ zone axis (b-i) and after a deliberate tilting away from pattern center following the red arrows (b-ii and b-iii). Marks (b): (expected) mirror planes (dashed lines), m—mirror plane, yellow circles emphasize absent mirror plane. (c) HRTEM micrograph of two domains oriented along the $[110]_C$ zone axis forming a superposition region separated by boundaries of superposition contrast (b1 and b2). Regions: (c-i, c-iii) Single crystalline domains, (c-ii) superposition. Marks: single domains (blue and red), the common intergrowth plane $\{111\}_C$ (dashed white line); fundamental reflections (white) and superposition reflections (yellow). (d) Overview HRSTEM micrograph with modulated (left) and unmodulated structure (right) along the $[112]_C$ zone axis, inset: magnified view of a 7L periodicity. (e) Reciprocal data set demonstrating a 1/7 $[111]_C$ modulation vector for the FFT pattern of the HRTEM micrograph (e-i) and a SAED pattern along the $[101]_C$ zone axis (e-ii) inset: magnified view of the periodicity. Marks: Growing direction along $[111]_C$ (white arrows), 7L periodicity (red arrows).

dimensional space group *pm*, [cf. Fig. 4(b-i)]. The pattern is oriented along the $[100]_c$ zone axis containing a single mirror plane assignable to $(001)_c$ or $(010)_c$. A verification of this finding was obtained by a deliberate tilt into perpendicular directions, respectively. Only in the tilt position of Fig. 4(b-ii) a mirror plane is detectable; in the other direction, a clear breakdown of the mirror symmetry becomes even more clearly [cf. marks in Fig. 4(b-iii)]. Consequently, several of the $\{110\}_c$ mirror planes were excluded analogously. The experimental findings allow the assumption of the space group *P4 mm* as an adequate candidate for the structure. On closer inspection, the expected symmetry of the CBED pattern is marginally violated. An interpretation of similar observations was provided by Tsuda *et al.* for BTO.[62] In these studies, CBED examinations indicated the presence of nanosized domains with different symmetries, e.g., local contributions of a coexisting trigonal (rhombohedral) phase.[37] Note that the experimental findings and the suggested presence of a morphotropic phase boundary (MPB)[33,63] can also be reasonably interpreted as a monoclinic symmetry (space group *Pm*). The recorded patterns, including mirror planes $(001)_c$ or $(010)_c$, would then be assigned to the monoclinic zone axes $[h0l]$ or $[0h\bar{l}]$. However, in the present investigations, clear evidence is missing for a monoclinic or trigonal symmetry.

The wedge shaped columns contain a complex substructure differentiating into twinned domains, cf. the HRTEM micrograph of Fig. 4(c) and the ED pattern in Fig. S4 of the supplementary material. In this special case, the corresponding Fourier transforms show two single crystalline domains oriented along $[110]_c$, which are mirrored along the $\{111\}_c$ planes, cf. domains (i) and (iii) of Fig. 4(c). Both domains are separated by boundaries b1 and b2, and these twinned domains seem to be superimposed along the viewing direction in region (ii) according to a three-dimensional inclined defect boundary model discussed in Fig. S2 of the supplementary material. Hence, b1 and b2 represent boundaries of superposition contrast. The FFT pattern of region (ii) appears as a superposition of the pattern from regions (i) and (iii), with Bragg intensities from pattern (iii) less pronounced and, thus, as minority component. Due to the superposition and the interrelated double diffraction phenomena, another group of intensities is observable, which is not assignable to one of the single domain patterns [see yellow marks in Fig. 4(c)]. The interpretation of these intensities and simulations of TEM data are based on supercells of superimposed twin domains.[64–66] Construction details of the supercell (Fig. S3 in the supplementary material) and respective experimental data with simulations for two experimentally observed scenarios, the edge-on view and special superposition case are provided in the supplementary material and are compared with each other (Fig. S4 in the supplementary material): (1) An experimental SAED pattern recorded on two adjacent single domains shows no indication of superposition contrast, thus, no superposition area is present. Only fundamental Bragg reflections of the respective single domains are visible matching excellently with the arrangement of the reflections in a kinematical simulation based on a supercell. Note, additional reflections seen in Fig. 4(c-ii) are absent. (2) Assuming a superposition of two $[110]_c$ oriented domains in a dynamical simulation, additional Bragg reflections can be generated agreeing with the experimental FFT pattern (Fig. S4 in the supplementary material). Thus, the additional Bragg intensities in the FFT are superposition

introduced features and are located on commensurable lattice positions of this pattern. The formation of polysynthetic $\{111\}$ growth twins is a well-known characteristic of the BTO bulk and thin films with a cubic or tetragonal symmetry.[67–69] Following the interpretation of previous studies the edge-on $\{111\}$-defect structure can be described as $\sum = 3$ twin boundary with coinciding (111) and $(\bar{1}12)$ reflections in ED patterns along the zone axis $[1\bar{1}0]$.[70–72] In the case of tetragonal BTO, the local arrangement of TiO_6 octahedra at the twin interface varies with respect to the bulk structure, i.e., corner-sharing TiO_6 ocatahedra are replaced by face-sharing Ti_2O_9-dimers. Such a local structure variation is supposed to accommodate for local oxygen deficiency.[73] These results can be analogously transferred to BCZT in many instances. However, to obtain in-depth information about the atomic configuration directly at the interface region, further aberration corrected HRTEM investigations are essential.

In some instances, lamellar fringes are detected propagating parallel to the Pt surface, which is expressed by an alternating bright-dark contrast. Preliminary EDX nanoprobe measurements excluded the diffusion of Pt into the fringe dominated areas and also variations of the composition on a larger scale. A high-resolution inspection of the fringed areas reveals a periodic arrangement of a seven layer (7L) sequence, cf. Fig. 4(d), featuring disturbances of locally different repetition schemes. By evaluating the corresponding FFT [Fig. 4(e-i)] and a correlated SAED pattern [Fig. 4(e-ii)], satellite intensities were observed, referring to a structural modulation[74] of the ideal pseudocubic structure. The modulation vector is close to $1/7 \, [111]_c$ as observed along different viewing directions, cf. the respective insets Fig. 4(e). Further, the magnified views of the diffraction pattern reveal an incommensurate arrangement of the satellite reflections, which is particularly visible in the SAED pattern indicating high order satellites. A polytypism[75] could serve as possible basis for the interpretation of the experimental findings and is discussed further in Fig. S5 in the supplementary material. In the literature, stoichiometric and oxygen-deficient polytypes were discussed for several perovskites or perovskite-related oxides.[76–78] A first set of experiments with a transmission electron microscope equipped with a Super-X EDX system for atomic resolution EDX was carried out to study the chemical composition with atomic resolution (see Fig. S6 in the supplementary material). However, a clear interpretation of the layer sequence of BCZT and the polytype was impossible from EDX data due to the overlap of the Ti-K and Ba-L peaks. *In situ* annealing experiments were performed exhibiting no significant change to the modulated structure during the entire process. Consequently, we assume that the modulated structure is not based on oxygen deficiency but homovalent cationic ordering on A- and B-sites. With respect to further investigations, the capabilities of aberration-corrected microscopy allow precise determination of the atomic configuration in PZT at the nanoscale.[79] Hence, an aberration-corrected HRTEM micrograph of BCZT is depicted in Fig. S7 in the supplementary material displaying pronounced contrast intensity variations on the cationic positions indicating the presence of cationic disordering compared to high-resolution simulations (Fig. S7-i in the supplementary material) based on the tetragonal (*P4 mm*) structure model (ii). Despite such ordering scheme, well known for relaxor materials, these structural domains

are not expected to produce the randomly oriented dipoles since their density is too low.

SUMMARY AND CONCLUSIONS

Ferroelectric lead-free thin films of the composition $(Ba_{0.85}Ca_{0.15})(Ti_{0.9}Zr_{0.1})O_3$ (BCZT) were deposited by pulsed laser deposition (PLD). The BCZT thin films are composed of columnar grains with preferred $[111]_C$ growth. We report a maximum of the dielectric permittivity of $\varepsilon = 2000$ at 5 khZ and a maximum effective piezoelectric constant of $d_{33,f} = 190\,\mathrm{pm/V}$, which could be improved to 300 pm/V. The temperature dependence of the permittivity on the frequency and deviation from the Curie-Weiss law indicates a relaxor behavior for the present thin films. CBED studies on single domains are consistent with a noncubic but tetragonal $P4$ mm symmetry. Additionally, inside the columns several microstructural characteristics were observed: (1) The presence of a modulation along the $[111]_C$ direction, and, a polytype with pronounced cation segregation was assumed as a potential interpretation. (2) Twinned domains with varying interconnection of the octahedral structural units. Transmitted areas with twinned domains show additional reflections which were proven to be excited by dynamical scattering and not by a potentially lower symmetry. All these characteristics are not interconnected with the microstructural origin of the relaxor effect, however, their presence complicate the identification of potential polar nanodomains.

SUPPLEMENTARY MATERIAL

See the supplementary material for additional information on physical and structural investigations performed during the study and referred to in the text.

ACKNOWLEDGMENTS

REFERENCES

[1] P. Muralt, J. Am. Ceram. Soc. **91**, 1385 (2008).

[2] R. G. Polcawich, J. S. Pulskamp, S. Bedair, G. Smith, R. Kaul, C. Kroninger, E. Wetzel, H. Chandrahalim, and S. A. Bhave, in *2010 IEEE Sensors* (New York, 2010), pp. 2193–2196.

[3] C.-B. Eom and S. Trolier-McKinstry, MRS Bull. **37**, 1007 (2012).

[4] S. Trolier-McKinstry and P. Muralt, J. Electroceram. **12**, 7 (2004).

[5] M. D. Maeder, D. Damjanovic, and N. Setter, J. Electroceram. **13**, 385 (2004).

[6] J. Rödel, W. Jo, K. T. P. Seifert, E.-M. Anton, T. Granzow, and D. Damjanovic, J. Am. Ceram. Soc. **92**, 1153 (2009).

[7] E. Aksel and J. L. Jones, Sensors **10**, 1935 (2010).

[8] S. Y. Lee, C. W. Ahn, J. S. Kim, A. Ullah, H. J. Lee, H.-I. Hwang, J. S. Choi, B. H. Park, and I. W. Kim, J. Alloys Compd. **509**, L194 (2011).

[9] X. J. Zheng, Y. F. Rong, D. Z. Zhang, T. Zhang, L. He, and X. Feng, Mater. Lett. **64**, 618 (2010).

[10] N. Ledermann, P. Muralt, J. Baborowski, S. Gentil, K. Mukati, M. Cantoni, A. Seifert, and N. Setter, Sens. Actuators A **105**, 162 (2003).

[11] W. Liu and X. Ren, Phys. Rev. Lett. **103**, 257602 (2009).

[12] P. Muralt, Integr. Ferroelectr. **17**, 297 (1997).

[13] K. Lefki and G. J. M. Dormans, J. Appl. Phys. **76**, 1764 (1994).

[14] N. Sama, C. Soyer, D. Remiens, C. Verrue, and R. Bouregba, Sens. Actuators A **158**, 99 (2010).

[15] D. Xue, Y. Zhou, H. Bao, C. Zhou, J. Gao, and X. Ren, J. Appl. Phys. **109**, 054110 (2011).

[16] E. A. Neppiras, J. Sound Vib. **20**, 562 (1972).

[17] G. Kang, K. Yao, and J. Wang, J. Am. Ceram. Soc. **95**, 986 (2012).

[18] Q. G. Chi, H. F. Zhu, J. C. Xu, X. Wang, J. Q. Lin, Z. Sun, Y. Chen, and Q. Q. Lei, Ceram. Int. **39**, 8195 (2013).

[19] A. Jalalian, A. M. Grishin, X. L. Wang, Z. X. Cheng, and S. X. Dou, Appl. Phys. Lett. **104**, 103112 (2014).

[20] B. C. Luo, D. Y. Wang, M. M. Duan, and S. Li, Appl. Phys. Lett. **103**, 122903 (2013).

[21] A. Piorra, A. Petraru, H. Kohlstedt, M. Wuttig, and E. Quandt, J. Appl. Phys. **109**, 104101 (2011).

[22] C. Bhardwaj and D. Kaur, Curr. Appl. Phys. **12**, 1239 (2012).

[23] Y. Lin, N. Qin, G. Wu, T. Sa, and D. Bao, Appl. Phys. A **109**, 743 (2012).

[24] T. Maiti, R. Guo, and A. S. Bhalla, Ferroelectrics **425**, 4 (2011).

[25] V. V. Shvartsman and D. C. Lupascu, J. Am. Ceram. Soc. **95**, 1 (2012).

[26] L. E. Cross, Ferroelectrics **76**, 241 (1987).

[27] A. J. Moulson and J. M. Herbert, *Electroceramics* (John Wiley & Sons, Ltd, Chichester, UK, 2003).

[28] D. Viehland, S. J. Jang, L. E. Cross, and M. Wuttig, J. Appl. Phys. **68**, 2916 (1990).

[29] A. A. Bokov and Z.-G. Ye, in *Frontiers of Ferroelectricity* (Berlin, 2006), pp. 31–52.

[30] K. Uchino and S. Nomura, Ferroelectrics **44**, 55 (1982).

[31] A. Dixit, S. B. Majumder, R. S. Katiyar, and A. S. Bhalla, J. Mater. Sci. **41**, 87 (2006).

[32] X. G. Tang, K.-H. Chew, and H. L. W. Chan, Acta Mater. **52**, 5177 (2004).

[33] J. Gao, D. Xue, Y. Wang, D. Wang, L. Zhang, H. Wu, S. Guo, H. Bao, C. Zhou, W. Liu, S. Hou, G. Xiao, and X. Ren, Appl. Phys. Lett. **99**, 092901 (2011).

[34] P. A. Stadelmann, Ultramicroscopy **21**, 131 (1987).

[35] R. Kilaas, J. Microsc. **190**, 45 (1998).

[36] D. S. Keeble, F. Benabdallah, P. A. Thomas, M. Maglione, and J. Kreisel, Appl. Phys. Lett. **102**, 092903 (2013).

[37] Y. Yang, Z. Wang, J.-F. Li, and D. Viehland, J. Nanomater. **2010**, e756319 (2010).

[38] M. Davis, M. Budimir, D. Damjanovic, and N. Setter, J. Appl. Phys. **101**, 054112 (2007).

[39] J. Ouyang, R. Ramesh, and A. L. Roytburd, Appl. Surf. Sci. **252**, 3394 (2006).

[40] W. Li, J. Hao, W. Bai, and J. Zhai, J. Solgel Sci. Technol. **66**, 220 (2013).

[41] N. Abt, R. Moazzami, and Y. Nissan-Cohen, Integr. Ferroelectr. **2**, 121 (1992).

[42] W. L. Warren, B. A. Tuttle, D. Dimos, G. Pike E, H. N. Al-Shareef, R. Ramesh, and J. T. J. Evans, Jpn. J. Appl. Phys. **35**, 1521 (1996).

[43] J. Lee, R. Ramesh, V. G. Keramidas, W. L. Warren, G. E. Pike, and J. T. Evans, Appl. Phys. Lett. **66**, 1337 (1995).

[44] G. E. Pike, W. L. Warren, D. Dimos, B. A. Tuttle, R. Ramesh, J. Lee, V. G. Keramidas, and J. T. Evans, Appl. Phys. Lett. **66**, 484 (1995).

[45] A. Gruverman, B. J. Rodriguez, A. I. Kingon, R. J. Nemanich, A. K. Tagantsev, J. S. Cross, and M. Tsukada, Appl. Phys. Lett. **83**, 728 (2003).

[46] A. K. Tagantsev and G. Gerra, J. Appl. Phys. **100**, 051607 (2006).

[47] Y. Liu, Z. Wang, A. S. Thind, T. Orvis, D. Sarkar, R. Kapadia, A. Y. Borisevich, R. Mishra, A. I. Khan, and J. Ravichandran, J. Vac. Sci. Technol. A **37**, 011502 (2019).

[48] H. Bao, C. Zhou, D. Xue, J. Gao, and X. Ren, J. Phys. D Appl. Phys. **43**, 465401 (2010).

[49] K. Prabahar, R. Ranjith, A. Srinivas, S. V. Kamat, B. Mallesham, V. L. Niranjani, J. P. Praveen, and D. Das, Ceram. Int. **43**, 5356 (2017).

[50] X.-G. Tang and H. L.-W. Chan, J. Appl. Phys. **97**, 034109 (2005).

[51] N. D. Scarisoreanu, F. Craciun, A. Moldovan, V. Ion, R. Birjega, C. Ghica, R. F. Negrea, and M. Dinescu, ACS Appl. Mater. Interfaces **7**, 23984 (2015).

[52]V. Ion, F. Craciun, N. D. Scarisoreanu, A. Moldovan, A. Andrei, R. Birjega, C. Ghica, F. Di Pietrantonio, D. Cannata, M. Benetti, and M. Dinescu, Sci. Rep. **8**, 2056 (2018).

[53]X. Dai, Z. Xu, J.-F. Li, and D. Viehland, J. Mater. Res. **11**, 618 (1996).

[54]W. Kleemann, J. Adv. Dielect. **02**, 1241001 (2012).

[55]A. Dixit, S. B. Majumder, R. S. Katiyar, and A. S. Bhalla, Appl. Phys. Lett. **82**, 2679 (2003).

[56]S. Yun, X. Wang, B. Li, and D. Xu, Solid State Commun. **143**, 461 (2007).

[57]P. Victor, R. Ranjith, and S. B. Krupanidhi, J. Appl. Phys. **94**, 7702 (2003).

[58]J. G. Park, T. S. Oh, and Y. H. Kim, J. Mater. Sci. **27**, 5713 (1992).

[59]P. S. R. Krishna, D. Pandey, V. S. Tiwari, R. Chakravarthy, and B. A. Dasannacharya, Appl. Phys. Lett. **62**, 231 (1993).

[60]M. Čeh and D. Kolar, Mater. Res. Bull. **29**, 269 (1994).

[61]C. Laulhé, A. Pasturel, F. Hippert, and J. Kreisel, Phys. Rev. B **82**, 132102 (2010).

[62]K. Tsuda, R. Sano, and M. Tanaka, Phys. Rev. B **86**, 214106 (2012).

[63]H. Wang, J. Zhu, N. Lu, A. A. Bokov, Z.-G. Ye, and X. W. Zhang, Appl. Phys. Lett. **89**, 042908 (2006).

[64]V. Hrkac, L. Kienle, S. Kaps, A. Lotnyk, Y. K. Mishra, U. Schürmann, V. Duppel, B. V. Lotsch, and R. Adelung, J. Appl. Crystallogr. **46**, 396 (2013).

[65]L. Kienle and A. Simon, J. Solid State Chem. **167**, 214 (2002).

[66]H.-J. Deiseroth, C. Reiner, K. Xhaxhiu, M. Schlosser, and L. Kienle, Z. Anorg. Allg. Chem. **630**, 2319 (2004).

[67]O. Eibl, P. Pongratz, and P. Skalicky, Philos. Mag. B **57**, 521 (1988).

[68]A. Rečnik, J. Bruley, W. Mader, D. Kolar, and M. Rühle, Philos. Mag. B **70**, 1021 (1994).

[69]C. L. Jia, Philos. Mag. Lett. **79**, 99 (1999).

[70]M. Fujimoto, J. Cryst. Growth **237–239**, 430 (2002).

[71]C. L. Jia, K. Urban, M. Mertin, S. Hoffmann, and R. Waser, Philos. Mag. A **77**, 923 (1998).

[72]C. L. Jia and A. Thust, Phys. Rev. Lett. **82**, 5052 (1999).

[73]C. L. Jia and K. Urban, Science **303**, 2001 (2004).

[74]G. King, S. Garcia-Martin, P. M. and Woodward, Acta Crystallogr. B **65**, 676 (2009).

[75]A. Guinier, G. B. Bokij, K. Boll-Dornberger, J. M. Cowley, S. Ďurovič, H. Jagodzinski, P. Krishna, P. M. de Wolff, B. B. Zvyagin, D. E. Cox, P. Goodman, T. Hahn, K. Kuchitsu, and S. C. Abrahams, Acta Crystallogr. **40**, 399 (1984).

[76]E. García-González, M. Parras, and J. M. González-Calbet, Chem. Mater. **11**, 433 (1999).

[77]H. Yang, Y. K. Tang, L. D. Yao, W. Zhang, Q. A. Li, F. Y. Li, C. Q. Jin, and R. C. Yu, J. Alloys Compd. **432**, 283 (2007).

[78]J.-G. Cheng, J. A. Alonso, E. Suard, J.-S. Zhou, and J. B. Goodenough, J. Am. Chem. Soc. **131**, 7461 (2009).

[79]K. W. Urban, Science **321**, 506 (2008).